Vol. 30 • No. 6 • February 8 • 2018

www.advmat.de

ADVANCED MATERIALS

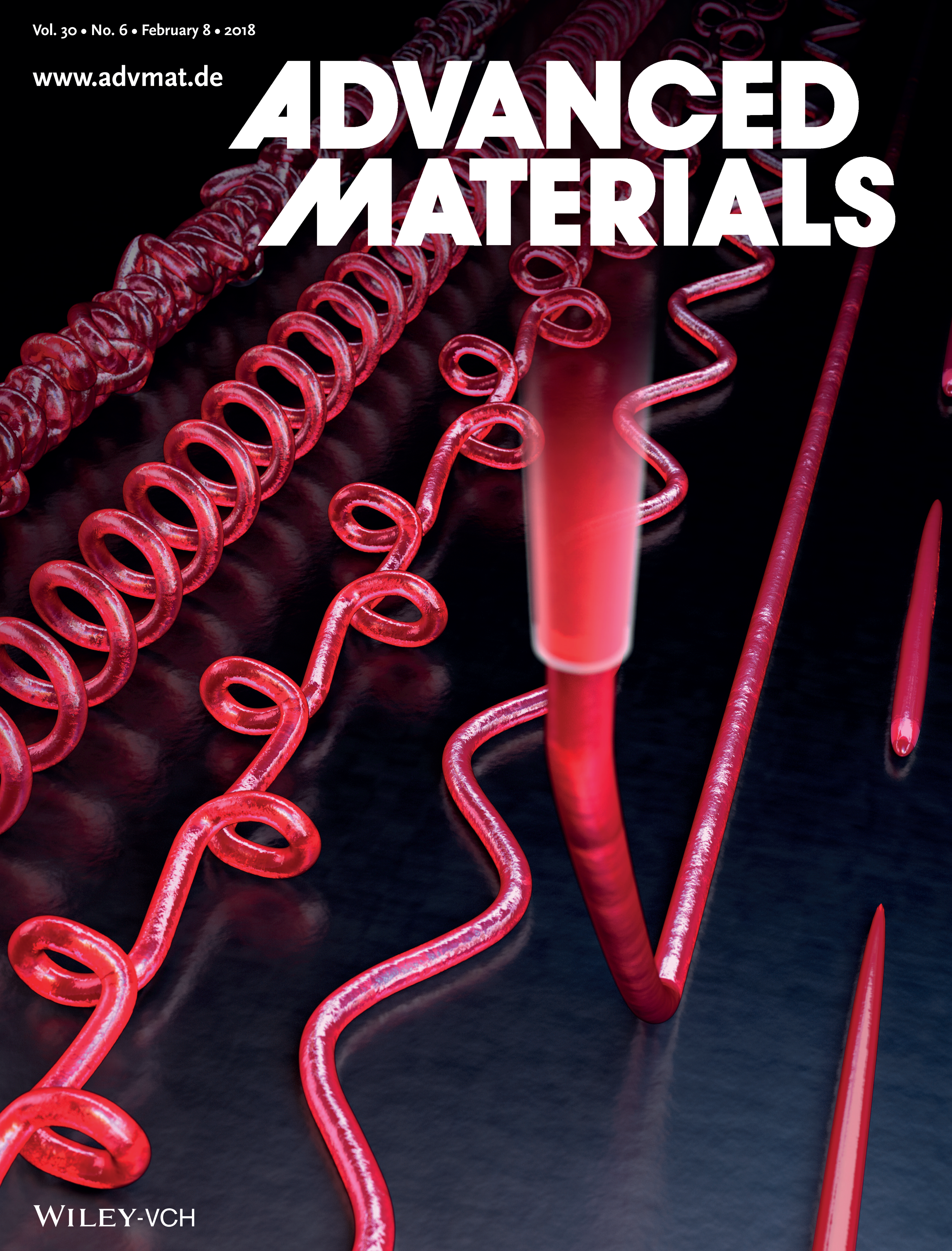

WILEY-VCH

A New 3D Printing Strategy by Harnessing Deformation, Instability, and Fracture of Viscoelastic Inks

*Hyunwoo Yuk and Xuanhe Zhao**

Direct ink writing (DIW) has demonstrated great potential as a multimaterial multifunctional fabrication method in areas as diverse as electronics, structural materials, tissue engineering, and soft robotics. During DIW, viscoelastic inks are extruded out of a 3D printer's nozzle as printed fibers, which are deposited into patterns when the nozzle moves. Hence, the resolution of printed fibers is commonly limited by the nozzle's diameter, and the printed pattern is limited by the motion paths. These limits have severely hampered innovations and applications of DIW 3D printing. Here, a new strategy to exceed the limits of DIW 3D printing by harnessing deformation, instability, and fracture of viscoelastic inks is reported. It is shown that a single nozzle can print fibers with resolution much finer than the nozzle diameter by stretching the extruded ink, and print various thickened or curved patterns with straight nozzle motions by accumulating the ink. A quantitative phase diagram is constructed to rationally select parameters for the new strategy. Further, applications including structures with tunable stiffening, 3D structures with gradient and programmable swelling properties, all printed with a single nozzle are demonstrated. The current work demonstrates that the mechanics of inks plays a critical role in developing 3D printing technology.

Direct ink writing (DIW) has demonstrated great potential as a versatile method to 3D print multimaterial and multifunctional structures for applications in diverse fields including stretchable electronics,[1,2] organ on a chip,[3,4] soft robotics,[5,6] biomedical implants,[7,8] and smart composites.[9–11] While the inks for DIW 3D printing span as diverse as conductive pastes,[1] elastomers,[5,7,11] and hydrogels;[2,4,10,12,13] they usually possess common rheological properties such as viscoelasticity, shear thinning, and yield stress flow to aid printing processes.[12–14] During DIW, pressurized viscoelastic inks are extruded out of the 3D printer's nozzles in form of printed fibers, which are deposited into patterns based on the prescribed motion of nozzles. In most DIW printing processes, a single set of printing conditions is adopted through trials and errors, and rarely changed during printing.[2,10,12,13] As a result, the resolution of printed fibers is usually limited by the nozzle's diameter, and the printed pattern is limited by the nozzle's motion paths. Such limitations have greatly restricted the versatility and applications of existing DIW 3D printing approaches.

Here, we report a new strategy to overcome the limits of DIW 3D printing by harnessing deformation, instability, and fracture of viscoelastic inks. We show that a single nozzle can print fibers with resolution much finer than nozzle diameter by stretching the extruded ink, and print various thickened or curved patterns with straight nozzle motions by accumulating the ink. To rationally select parameters for the new printing strategy, we construct a phase diagram to quantitatively guide deformation, instabilities, and fracture of viscoelastic inks. This new strategy provides a wide new avenue to opportunities beyond the limits of existing DIW 3D printing approaches. We also demonstrate novel applications of the new 3D printing strategy including stretchable structures with tunable stiffening and 3D structures with gradient properties, and programmable swelling properties, all printed with a single nozzle.

Figure 1a schematically illustrates the typical setup and parameters for DIW 3D printing. The viscoelastic ink is extruded out of the nozzle tip, with inner diameter D, at a speed of C (without deformation). The extrusion of the viscoelastic inks usually leads to die-swelling of the inks,[15] resulting in printed fibers with diameter αD, where α is a die-swelling ratio greater than unity. Therefore, the extrusion rate (or feed rate) due to the volume conservation is $Q = \pi C(\alpha D)^2/4$. The nozzle tip moves at a speed of V and a height of H (from the surface of substrate or printed layers) while depositing fibers of the viscoelastic ink. In convectional DIW 3D printing, the moving speed of the printer nozzle V is set to be equal to C. As a result, the resolution of printed fibers is limited to αD, and the printed pattern is controlled by the continuous motion path of the nozzle. Note that C is typically determined by ink's material properties and applied pressure P during DIW 3D printing.

In this study, we will show that (i) a single nozzle can print fibers with various diameters much smaller than αD, significantly enhancing the resolution of DIW printing; (ii) the printed fiber can be discontinuous despite the continuous motion of the nozzle; and (iii) complex patterns of printed fibers can be achieved with simple straight nozzle motions. In the subsequent analysis, we will control two nondimensionalized printing parameters to develop the new DIW 3D printing

H. Yuk, Prof. X. Zhao
Soft Active Materials Laboratory
Department of Mechanical Engineering
Massachusetts Institute of Technology
Cambridge, MA 02139, USA
E-mail: zhaox@mit.edu
Prof. X. Zhao
Department of Civil and Environmental Engineering
Massachusetts Institute of Technology
Cambridge, MA 02139, USA

DOI: 10.1002/adma.201704028

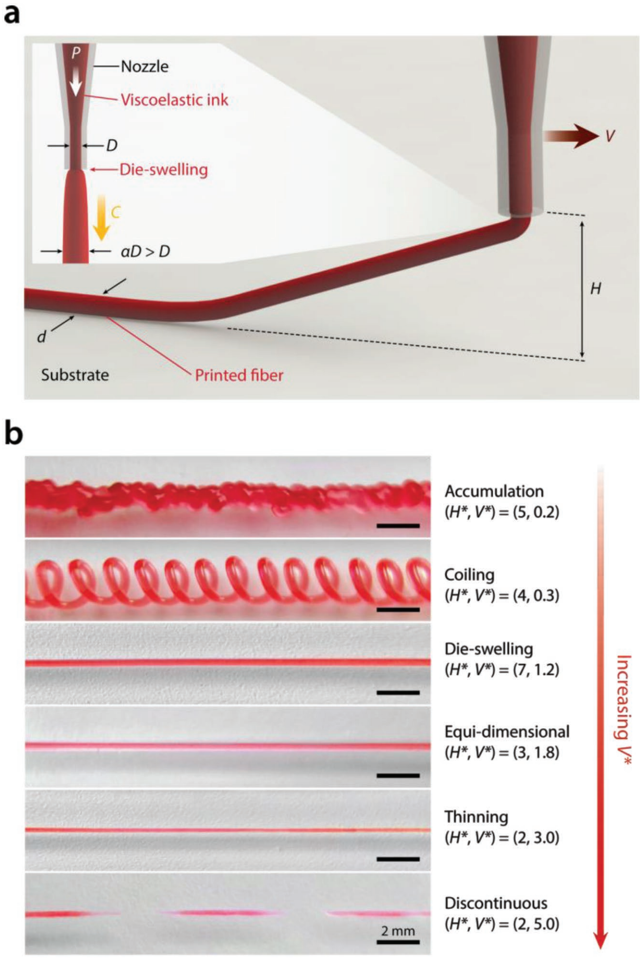

Figure 1. DIW 3D printing of viscoelastic inks. a) Schematic illustration of typical setup and parameters for DIW 3D printing. The viscoelastic ink is extruded out of the nozzle tip, with inner diameter D, at a speed of C while the nozzle tip moves at a speed of V and a height of H. b) Diverse modes in new 3D printing strategy by varying selections of printing parameters. Fibers with resolution unlimited by the nozzle diameter can be achieved in a highly controllable manner.

strategy: the nondimensional nozzle speed V^* and nondimensional nozzle tip height H^*, defined as

$$V^* \equiv \frac{V}{C} \tag{1a}$$

$$H^* \equiv \frac{H}{\alpha D} \tag{1b}$$

In conventional DIW 3D printing, the printing parameters V^* and H^* are commonly set to be unity, so that the extruded viscoelastic ink is deposited without significant deformation. In the new strategy, we will tune V^* and H^* in wide ranges to exploit deformation, instability, and fracture of viscoelastic inks, enabling new modes of DIW 3D printing including accumulation, coiling, die-swelling, equidimensional, thinning, and discontinuous modes (Figure 1b). As illustrated in Figure 1b, the new 3D printing strategy can give continuous and discontinuous fibers with diameters much finer than nozzle diameter (e.g., thinning and discontinuous modes), and nonlinear complex patterns of the fibers (e.g., coiling and accumulation modes) with a single nozzle. To accurately control different modes of printing, conditions for each mode and the corresponding printing parameters need to be quantitatively identified in a reproducible and predictable manner.

In the new strategy of DIW 3D printing, the effects of gravitational stretching and inertia are negligible (see Figures S1 and S2a of the Supporting Information).[16–18] Under such conditions, previous studies have shown that the coiling instability occurs when $V \le U_c$, where U_c is the steady coiling speed defined as $U_c \equiv R_c\Omega_c$ with R_c the radius of steady coiling and Ω_c the angular speed of the steady coiling (Figure S2b, Supporting Information).[16–20] Notably, the negligible gravitation stretching renders that the speed of ink extrusion is identical to the steady coiling velocity, $U_c = C$.[16] Therefore, the condition of coiling instability is $V \le C$, which renders $V^* \le 1$, given that H^* is large enough to avoid accumulation of the printed ink. The geometric model of coiling instability[18,20] also provides the corresponding ranges of V^* for each submode of printing: translating coiling ($0 < V^* < 0.33$); alternating coiling ($0.28 < V^* < 0.6$); stretching coiling ($0.55 < V^* < 0.68$); and meandering ($0.53 < V^* < 1$).

When the gravitation stretching is negligible, the radius of steady coiling scales with the nozzle tip height, $R_c \approx H$, and therefore, $\Omega_c \approx C/H$.[16] With this relation, the translational movement of the nozzle during each cycle of coiling can be expressed as $V\,\Delta t$, where $\Delta t \approx 1/\Omega_c$ (Figure S2c, Supporting Information).[16,17] As illustrated in Figure S2c of the Supporting Information, the coiled fibers will overlap each other when the translational movement is smaller than the printed fiber diameter, $V\Delta t \le \alpha D$, resulting in merging between the printed fibers and accumulation of the deposited ink. Therefore, the condition for the accumulation mode of printing can be expressed as

$$V^* \le \frac{1}{H^*} \quad \text{for accumulation mode} \tag{2}$$

where the diameter of printed fiber $d = \alpha D/\sqrt{V^*}$ (calculated from the volume conservation of the extruded ink) can be much greater than nozzle inner diameter D due to the accumulation of ink. Since the boundary between accumulation and coiling mode is given as $V^* = 1/H^*$, the complete condition for the coiling mode of printing becomes

$$\frac{1}{H^*} < V^* < 1 \quad \text{for coiling mode} \tag{3}$$

where the diameter of printed fiber d is equal to the die-swollen diameter αD (Figure S2a, Supporting Information). (Note that the coiling mode requires $H^* > 1$ since the deposited ink will be squeezed between the nozzle tip and the substrate or printed layers when $H^* \le 1$.)

When $V^* > 1$, the extruded viscoelastic ink starts to get stretched due to the motion of the nozzle (Figure S3a, Supporting Information).[21] Figure S3b of the Supporting Information schematically illustrates the stretching mode of printing

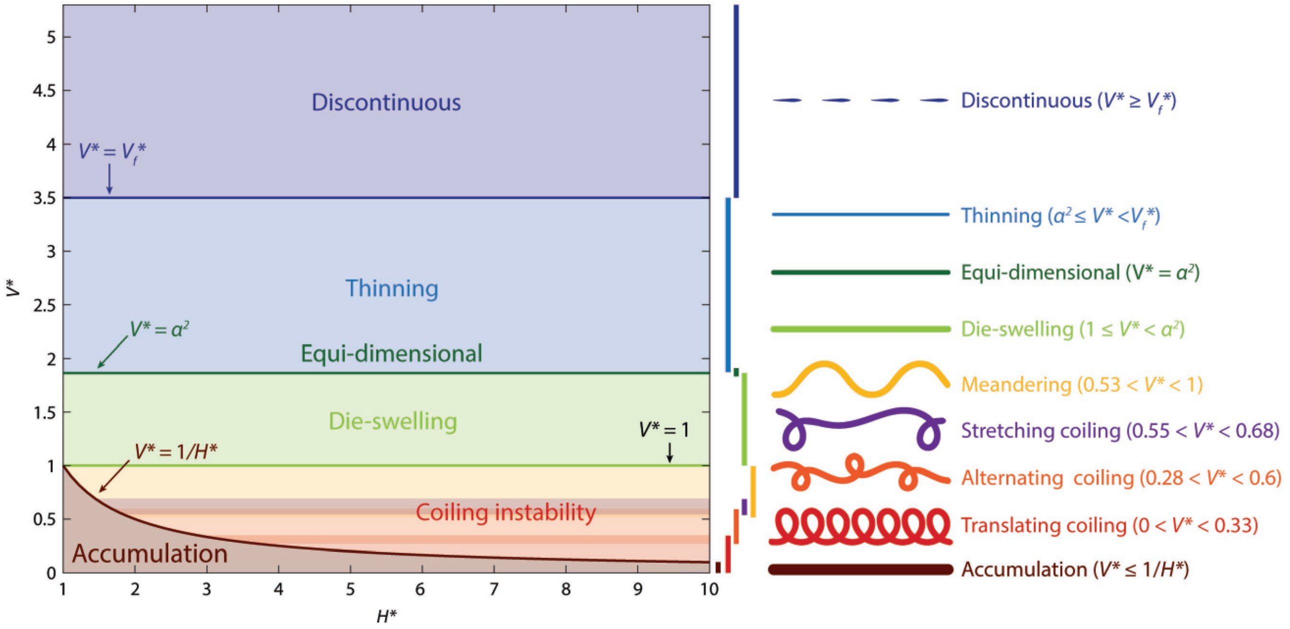

Figure 2. Phase diagram for the new strategy. A quantitative phase diagram to guide the selection of printing modes of viscoelastic inks governed by nondimensional parameters (H^*, V^*). Based on the phase diagram, different modes of DIW 3D printing of viscoelastic inks can be selected in a highly predictable manner. Schematic illustrations on the right of the phase diagram show shapes of the printed fibers for each mode with the corresponding printing parameters.

with corresponding geometric parameters. The geometric consideration and the volume conservation of the extruded ink provide that the stretch ratio is the same as V^* with the stretching angle $\theta = \arccos\left(\frac{V^*-1}{V^*}\right)$ which agrees reasonably well with the experimental data for $H^* = 2$, 4, and 6 (Figure S3c, Supporting Information). Moreover, the corresponding true strain ε and true strain rate $\dot{\varepsilon}$ are $\varepsilon = \ln V^*$ (with respect to the printed fiber length without stretching) and $\dot{\varepsilon} = \frac{C}{\alpha D}\frac{1}{H^*}\ln V^*$, respectively. Assuming incompressibility and volume conservation of the extruded ink, the diameter of the printed fiber can be calculated as $d = \alpha D/\sqrt{V^*}$. According to the normalized nozzle speed, the thinning mode of printing can be classified as

$$1 \leq V^* < \alpha^2 \quad \text{for die-swelling mode} \tag{4}$$

where the die-swelling effect is dominant and the diameter of printed fiber d is greater than nozzle inner diameter D.

$$V^* = \alpha^2 \quad \text{for equidimensional mode} \tag{5}$$

where the diameter of printed fiber d is equal to nozzle inner diameter D.

$$\alpha^2 < V^* < V_f^* \quad \text{for thinning mode} \tag{6}$$

where the diameter of printed fiber d can be much smaller than nozzle inner diameter D, enhancing the resolution of the printing. In Equation (6), V_f^* is the nondimensional nozzle speed at which the extruded ink starts to undergo fracture. Hence, the upper limit of the thinning mode is given as $V^* = V_f^*$. Note that V_f^* is a material property, given that the Weissenberg number is greater than one (see Supporting Information).[22] For example, the experimental measurements give $V_f^* \approx 3.5$ for a silicone elastomer ink (SE 1700; Dow Corning and Dragon Skin; Smooth-On), and $V_f^* \approx 30$ for a hydrogel ink (polyethylene oxide (PEO) solution) (see Experimental Section). Therefore, by adopting the thinning mode of printing, the resolution of the printed fibers can be enhanced up to 1.9 and 5.4 times for the silicone elastomer and the hydrogel inks, respectively.

When the nozzle speed exceeds V_f^*, the thinning of extruded ink by stretching transits to the fracture of stretched ink, resulting in discontinuous patterns of printed fiber segments (Figure S4a, Supporting Information). Hence, the condition for the discontinuous mode of printing can be expressed as

$$V_f^* \leq V^* \quad \text{for discontinuous mode} \tag{7}$$

where the diameter of printed fiber d reaches its minimum value $\alpha D/\sqrt{V_f^*}$ as the fiber cannot be further stretched.

Based on the conditions for various modes of DIW 3D printing, we construct a quantitative phase diagram with nondimensional printing parameters (H^*, V^*) to guide rational selection of parameters for the new strategy (**Figure 2**). To experimentally validate the new 3D printing strategy, we perform a systematic set of experiments for various combinations of H^* and V^* with the silicone elastomer ink (SE 1700; Dow Corning and Dragon Skin; Smooth-On) as a model material for commonly used viscoelastic inks in DIW 3D printing. The printed fibers under different conditions of H^* and V^* are illustrated in **Figure 3**a, with the corresponding modes of printing summarized in Figure 3b. The experimental data show

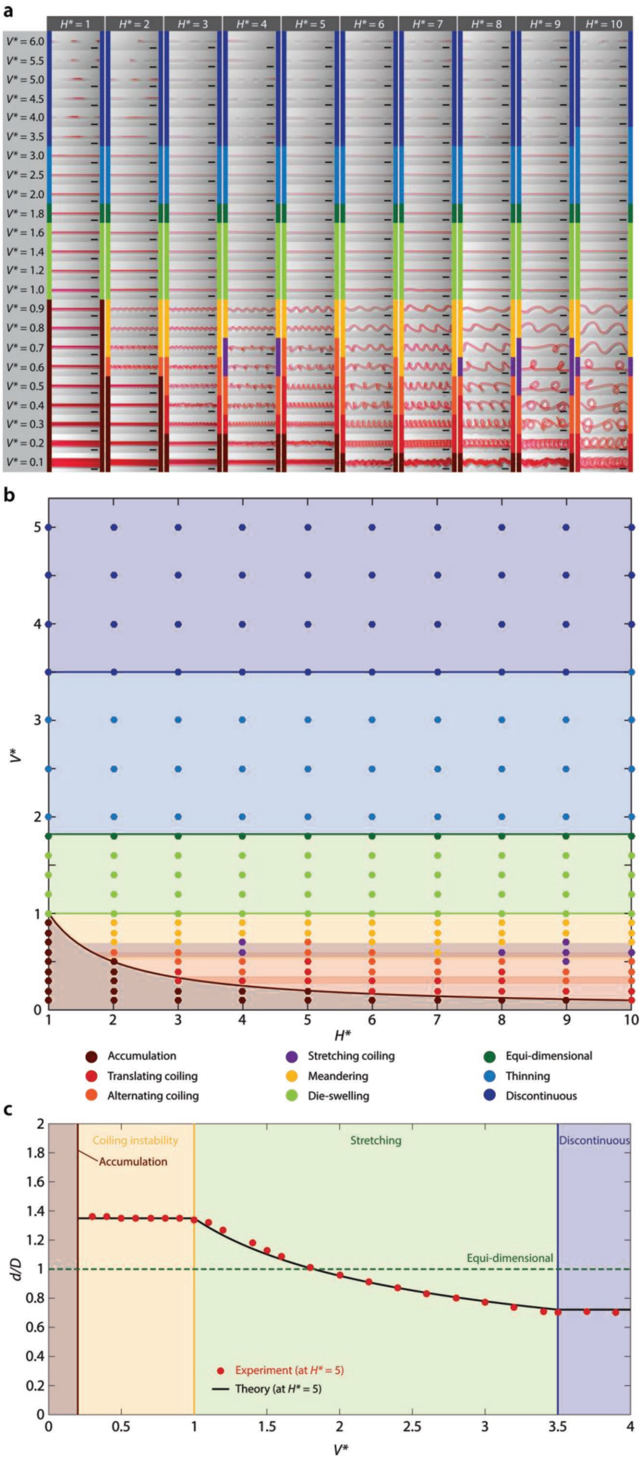

Figure 3. Experimental validation of the phase diagram. a) Experimental images for the printed fibers with various selections of printing parameters (scale bars: 2 mm). b) Experimental data plotted in the phase diagram. c) d/D as a function of V^* at $H^* = 5$. Dots represent experimental data, and the solid curve represents the theoretical prediction.

good agreement with the phase diagram, validating the proposed strategy. Also, the printed fiber diameter can be predicted reasonably well over various printing modes and parameters, further demonstrating the enhanced resolution of DIW printing much beyond the nozzle diameter in highly predictable manner (Figure 3c).

Next, we show the capability of using a single nozzle to print fibers with various diameters (unlimited by nozzle diameter) and complex patterns with straight nozzle motions by adopting new modes of DIW 3D printing. Furthermore, the transition between different modes can be continuous, enabling the continuous printing of various nonlinear patterns and fiber diameters by one nozzle in undisrupted manner. In one example, we program parallel straight paths of the nozzle motion with different values of V^* (0.1, 0.4, 0.8, 1.1, 1.8, 2.5, and 5.0) and $H^* = 5$ for each path (**Figure** 4a). Aided by the phase diagram, various modes of printing and their corresponding nonlinear patterns and fiber diameters can be achieved in highly reproducible manner (Figure 4b; Video S1, Supporting Information). In another example, we continuously vary the speed and the height of the nozzle from $V^* = 0.3$ to 2.5 and $H^* = 5$ to 2 (Figure 4a) along a straight motion path of the nozzle. As a result, we can continuously print different modes (from coiling to thinning) and fiber diameters (from $d = 270$ to 170 µm) in a single fiber without disrupting the printing process or the nozzle motion path (Figure 4c).

The capability of tuning fiber diameters in highly reproducible and predictable manner further enables us to print 3D solid structures with varying resolutions and layer thicknesses using a single nozzle. In **Figure 5**a and Video S2 of the Supporting Information, we program continuous single-nozzle printing sequences to print fully filled 3D solid pyramids with different resolutions and layer thicknesses by tuning fiber diameters via adopting accumulation ($d = 420$ µm with $(H^*, V^*) = (1.5, 0.4)$), equidimensional ($d = 200$ µm with $(H^*, V^*) = (1.5, 1.8)$), and thinning ($d = 150$ µm with $(H^*, V^*) = (1, 3.2)$) modes of printing. The flexibility of the new strategy even allows us to change fiber diameters during the continuous printing process of a single solid structure as shown in Figure 5b and Video S2 of the Supporting Information.

Importantly, since the new strategy is based on the mechanics of viscoelastic inks, it can be readily applied to a wide range of viscoelastic inks. For instance, we select different values of V^* (0.3, 0.6, 0.8, 1.5, 3, 10, 25, and 30) for $H^* = 4$ to print several lines with straight nozzle motions for the hydrogel ink (PEO solution) (Figure S5, Supporting Information). While the coiled patterns have been adopted in the previous DIW 3D printing approaches;[23] to our best knowledge, this is the first demonstration of DIW 3D printed fibers with resolution much finer than the nozzle diameter (for example, up to 1.9 and 5.4 times for the silicone elastomer and the hydrogel inks, respectively) and discontinuous patterns in highly predictable and reproducible manner by following the quantitative phase diagram.

With the new 3D printing strategy, various novel applications and functionalities become accessible beyond the limits of conventional DIW 3D printing. For example, the ability to print diverse complex patterns with linear nozzle paths by coiling instability would open new avenues to fabricate stretchable structures with tunable stiffening properties. Delayed stiffening under deformation is frequently observed in many biological tissues, and play critical roles in their functionalities

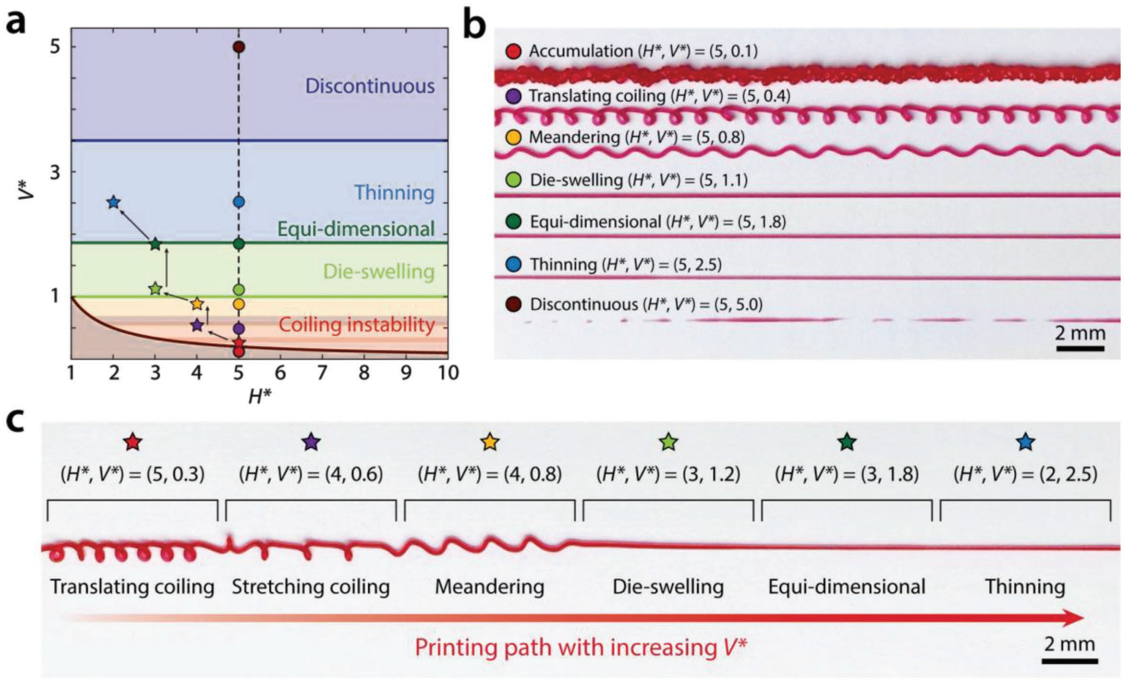

Figure 4. Predictable and reproducible printing of various fibers and patterns by a single nozzle. a) The phase diagram with marked symbols (solid circle or star) for corresponding printing parameter selections. b) Single nozzle printing of fibers with various diameters and complex patterns with parallel straight nozzle motions by adopting the new modes of DIW 3D printing. Each printing condition corresponds to solid circle symbols along the dotted line in (a). c) Single nozzle printing of various nonlinear patterns and fiber diameters in a single printed fiber by continuous transition between different modes. Each printing condition corresponds to solid star symbols in (a).

and structural robustness.[24] In nature, such property is typically achieved by straightening and consequent stiffening of the folded collagen fibers under tension.[25] In engineering applications, similar approaches have been applied in a wide range of fields such as stretchable electronics,[26] but fabrication of such structures usually requires complicated multistep processes in small scales.[27] In contrast, we demonstrate that stretchable structures with tunable stiffening property can readily be printed by harnessing instability of the viscoelastic ink (**Figure** 6a–c). During the coiling mode of printing ($1/H^* < V^* \leq 1$), the total length of the printed fiber becomes $1/V^*$ times of the translational movement of the nozzle tip due to the coiling instability. To straighten the resultant wavy fiber, it should be stretched to $\lambda = 1/V^*$ during which tensile resistance is very low, resulting in the delayed stiffening under tension (Figure S6, Supporting Information). Hence, the locking stretch of the printed fiber can be expressed as

$$\lambda_L = \lambda_{L0}/V^* \tag{8}$$

where λ_{LO} is the locking stretch of the fiber printed at $V^* = 1$. As shown in Figure 6a, the stiffening response of the printed fiber can be tuned in highly predictable manner by selecting appropriate printing parameters based on the phase diagram. In addition, the same approach can realize structures with anisotropic stiffening property in different directions, all printed with a single nozzle. In one example, we select $V^* = 0.8$ for both x and y directions, resulting in the delayed stiffening responses in both directions (Figure 6b). In another example, we select $V^* = 1.8$ for x direction (equidimensional mode) while $V^* = 0.8$ for y direction, resulting in the delayed stiffening response only in y direction (Figure 6c).

We can also achieve 3D structures with gradient properties by the new 3D printing strategy. In conventional DIW, printing of fibers with large range of diameters typically requires individually accessible nozzles with different diameters.[11,13] Thanks to predictable control of fiber diameter in the new 3D printing strategy, we can print a wide range of fiber diameters without changing the nozzle only by selecting appropriate printing parameters. Such gradient structures can be printed within the same layer of fibers by varying H^* and V^* when printing different fibers. For example, we vary V^* from 0.4 to 3.2 within the same layer to print a gradient mesh with the fiber diameter ranging from 420 to 150 µm (Figure 6d). The gradient can also be introduced over different layers in 3D structure by using different H^* and V^* in different layers. For example, we select $(H^*, V^*) = (4, 0.8)$ for the first layer, $(H^*, V^*) = (3, 1.2)$ for the second layer, $(H^*, V^*) = (3, 1.8)$ for the third layer, and $(H^*, V^*) = (2, 2.5)$ for the fourth layer to print a 3D structure with different patterns and fiber diameters for each layer (Figure S7 and Video S3, Supporting Information). In another example, we select $(H^*, V^*) = (1.5, 1)$ for layer 1 to 4 and $(H^*, V^*) = (0.7, 3)$ for layer 5 to 8 to print a 3D mesh with 8 layers (Figure 6e; Video S4, Supporting Information).

In addition, such structures can also have gradient kinetic properties that enables novel functions. For example, fibers with different diameters have different equilibrium swelling time t, following the quadratic diffusion relation $t \approx d^2$; and the diameter of fibers can be accurately controlled by the phase diagram (Figure S8, Supporting Information). Based on this, we design

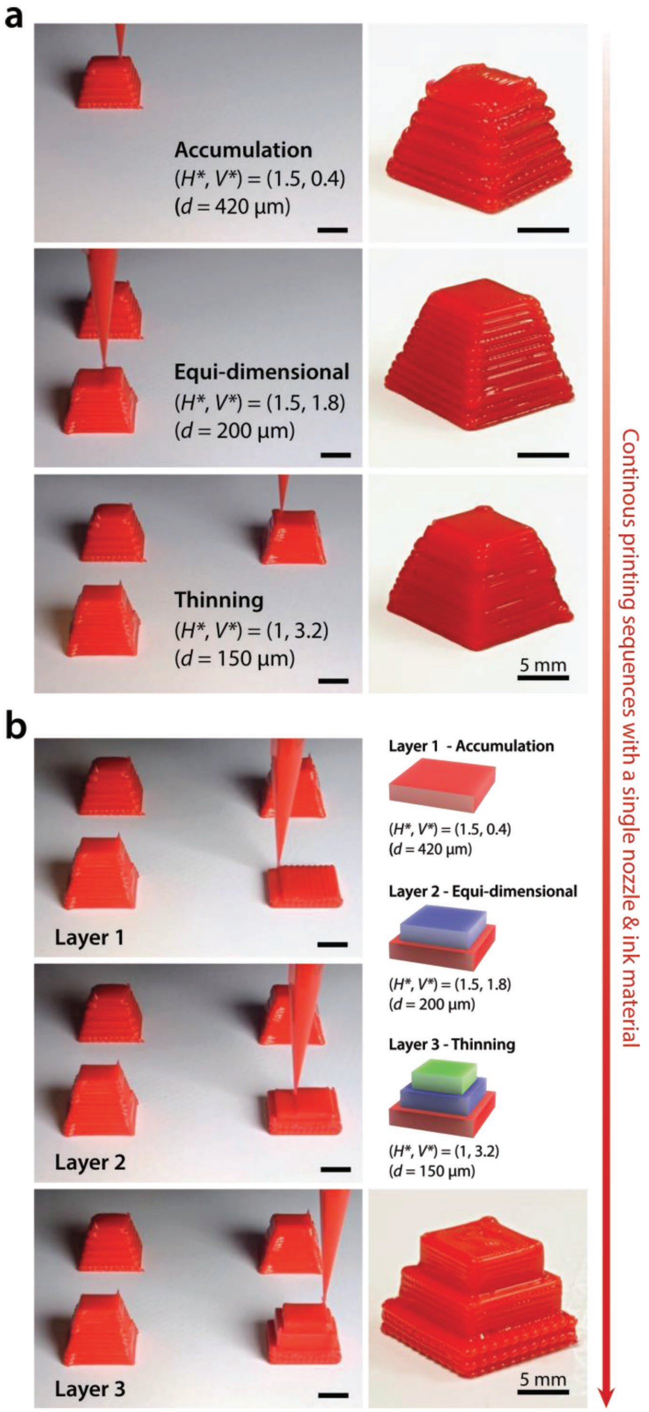

Figure 5. Printing of solid structures with varying fiber diameters by a single nozzle. a) Single nozzle printing of solid structures with varying fiber diameters in continuous printing sequences. b) Continuous single nozzle printing of a solid three-layered structure with different fiber diameters at each layer.

a swelling actuator with a gradient 3D mesh with two different fiber diameters in upper and lower part of the structure, all printed by a single nozzle (Figure 6e,f). When the actuator swells in a solvent (tetrahydrofuran), it initially buckles toward one side and gradually becomes flat over time (Figure 6f,g; Video S5, Supporting Information). This is because the part with smaller fiber diameter swells faster (d = 155 μm and $t \approx 20$ s) than the part with larger fiber diameter (d = 270 μm and $t \approx 80$ s) and both parts have the same equilibrium swelling ratio.

In summary, we introduce a new 3D printing strategy that can exceed the limits of existing DIW 3D printing by harnessing deformation, instability and, fracture of viscoelastic inks. We construct a quantitative phase diagram to provide highly predictable and reproducible rational guide for selection of printing parameters with experimental validations. This versatile DIW 3D printing strategy provides new ways of achieving much higher printing resolution beyond the nozzle diameter as well as various nonlinear patterns printed continuous motion paths by using a single nozzle. The new strategy can be applied to a wide range of viscoelastic ink materials for DIW 3D printing. With this capability beyond the conventional DIW 3D printing approaches, the new 3D printing strategy will be broadly applicable and impactful for diverse fields of science and engineering. In addition, the current work demonstrates that the mechanics of inks plays a critical role in developing 3D printing technology.

Experimental Section

Ink Preparation: Silicone elastomers, Dragon Skin 30 (Smooth-On) and SE 1700 (Dow Corning), were mixed together to form 3D printable viscoelastic ink. More specifically, Dragon Skin 30 part A, Dragon Skin 30 part B, SE 1700 base, and SE 1700 catalyst were added with 1:1:1:0.1 weight ratio and mixed thoroughly using a Thinky mixer (AR-100, Thinky) in a closed container. For images in the figures, red pigment for silicone elastomers (Smooth-On) was added in 1 wt% of the total elastomer mixture. To avoid changes in rheological properties, the prepared ink was used within 3 h after preparation. For the viscoelastic hydrogel ink in Figure S5 of the Supporting Information, 20 wt% of 900 kDa PEO (Sigma-Aldrich) was dissolved in deionized water. For images in the figure, fluorescein sodium salt (Sigma-Aldrich) was added in 0.1 wt% of the total hydrogel solution.

Rheological Characterizations: Rheological properties of inks were measured via rotational rheometer (AR-G2, TA Instruments) with 20 mm diameter steel plate. Complex moduli of inks were measured by small amplitude oscillatory shear tests over angular frequency range of 0.01–100 rad s^{-1} with oscillatory strain of 0.02. The master curve at the reference temperature of 25 °C was obtained by time temperature superposition method. The measured complex moduli were fitted with a Maxwell relaxation spectrum with five modes by MATLAB (Figure S1a, Supporting Information). The zero-shear viscosity η_0 was calculated from the Maxwell relaxation spectrum as $\eta_0 = \sum_{i=1}^{5} g_i \lambda_i$ where g_i is elastic modulus of ith mode and λ_i is relaxation time of ith mode. Apparent shear viscosity was obtained by steady-state flow tests with a logarithmic sweep of shear rate (0.01– 100 s^{-1}) (Figure S1b, Supporting Information). Yield stress flow behavior was characterized by oscillation tests with a logarithmic sweep of shear stress (1–1000 Pa) at 1 Hz shear frequency and oscillatory strain of 0.02 (Figure S1c, Supporting Information). All rheological measurements were conducted at 25 °C with preliminary equilibration time of 1 min.

Printing of Viscoelastic Inks: Print paths were generated via production of G-code that controls the XYZ motion of the 3D robotic gantry (Aerotech). G-code was either generated by manual coding or open-source software (Slic3r). Printing parameters (i.e., H and V) in G-codes were applied based on the phase diagram. Pressure based microdispensers (Ultimus V, Nordson EFD) were used to print inks via

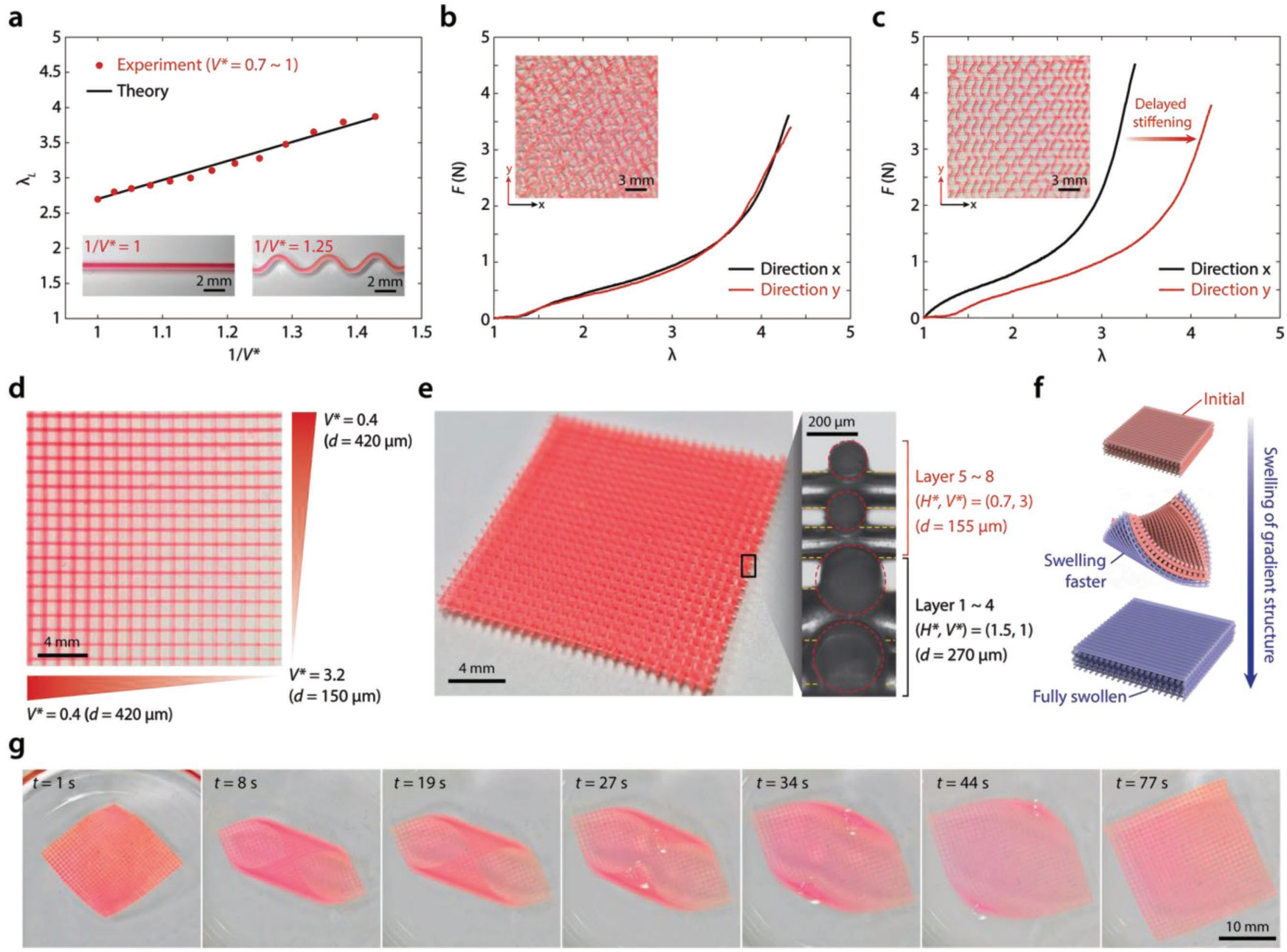

Figure 6. Novel functions enabled by the new 3D printing strategy. a) Plot of locking stretch λ_L of the printed fibers as a function of $1/V^*$ under simple tension. b) Plot of force F as a function of stretch λ for the 3D printed mesh with meandering pattern in both x and y directions. c) Plot of force F as a function of stretch λ for the 3D printed mesh with meandering pattern in only y direction. d) Single nozzle printing of a gradient mesh structure with varying fiber diameters within the same layer. e) Single nozzle printing of a gradient 3D structure with varying fiber diameters over different layers. f) Schematic illustration of swelling of a gradient 3D structure realized by the new 3D printing strategy. g) Inhomogeneous swelling response of the gradient actuator in an organic solvent (THF).

the custom LabVIEW interface (National Instruments). Inks were printed on silicon wafer or glass substrate coated with a nonadhesive release agent (MS-122AD, Miller-Stephenson) and cured in the oven at 120 °C for 30 min. Nozzles with various diameters were used including 50 µm (FISNAR), 100 µm (FISNAR), 200 µm (Nordson EFD), and 400 µm (Nordson EFD). 200 µm nozzle was used in experiments otherwise mentioned. The pressure of 200 kPa was used to dispense inks for all sizes of nozzles.

Mechanical Testing for Delayed Stiffening Structures: Tension tests of the printed samples were performed by the mechanical testing machine (20 N load cell; Zwick/Roell Z2.5) with 0.01 s^{-1} nominal strain rate. Nominal stress and stretch were calculated based on the initial specimen dimensions. The locking stretch of the samples was experimentally determined by examining the stretch level at which the slope of nominal stress versus stretch curve sharply increased (Figure S6, Supporting Information).

Measurement of Printed Fiber Diameter: The diameter of the printed fiber as a function of height was determined by optical micrometer (LS-7010, Keyence) (Figure S2a, Supporting Information). The diameter of printed fibers on substrates was measured by optical microscope (LV100ND, Nikon) (Figure 3c). For more accurate measurement of the fiber diameters, green fluorescent pigment for silicone elastomers (Smooth-On) was added in 1 wt% of the total elastomer mixture and imaged by the optical microscope with green fluorescence filter.

Swelling Test of Gradient 3D Structures: The swelling of 3D printed elastomer structure was performed by using organic solvent, tetrahydrofuran (THF, Sigma Aldrich). Swelling kinetics of fibers with different diameters were measured under optical microscope (LV100ND, Nikon). Upon the application of THF, equilibrium swelling time for each fiber was recorded and fitted using MATLAB (Figure S8, Supporting Information).

Supporting Information

Supporting Information is available from the Wiley Online Library or from the author.

Acknowledgements

This work was supported by ONR (No. N00014-17-1-2920), MIT Institute for Soldier Nanotechnologies and NSF (No. CMMI-1661627). H.Y. acknowledges the financial support from Samsung Scholarship.

Conflict of Interest

The authors declare no conflict of interest.

Keywords

3D printing, elastomers, hydrogels, mechanics, soft materials

Received: July 19, 2017
Revised: October 22, 2017
Published online: December 14, 2017

---

[1] a) B. Y. Ahn, E. B. Duoss, M. J. Motala, X. Guo, S.-I. Park, Y. Xiong, J. Yoon, R. G. Nuzzo, J. A. Rogers, J. A. Lewis, *Science* **2009**, *323*, 1590; b) J. T. Muth, D. M. Vogt, R. L. Truby, Y. Mengüç, D. B. Kolesky, R. J. Wood, J. A. Lewis, *Adv. Mater.* **2014**, *26*, 6307.

[2] K. Tian, J. Bae, S. E. Bakarich, C. Yang, R. D. Gately, G. M. Spinks, Z. Suo, J. J. Vlassak, *Adv. Mater.* **2017**, *29*, 1604827.

[3] a) H.-W. Kang, S. J. Lee, I. K. Ko, C. Kengla, J. J. Yoo, A. Atala, *Nat. Biotechnol.* **2016**, *34*, 312; b) J. S. Miller, K. R. Stevens, M. T. Yang, B. M. Baker, D.-H. T. Nguyen, D. M. Cohen, E. Toro, A. A. Chen, P. A. Galie, X. Yu, *Nat. Mater.* **2012**, *11*, 768; c) J. U. Lind, T. A. Busbee, A. D. Valentine, F. S. Pasqualini, H. Yuan, M. Yadid, S.-J. Park, A. Kotikian, A. P. Nesmith, P. H. Campbell, J. J. Vlassak, J. A. Lewis, K. K. Parker, *Nat. Mater.* **2017**, *16*, 303.

[4] D. B. Kolesky, K. A. Homan, M. A. Skylar-Scott, J. A. Lewis, *Proc. Natl. Acad. Sci. USA* **2016**, *113*, 3179.

[5] M. Wehner, R. L. Truby, D. J. Fitzgerald, B. Mosadegh, G. M. Whitesides, J. A. Lewis, R. J. Wood, *Nature* **2016**, *536*, 451.

[6] D. Rus, M. T. Tolley, *Nature* **2015**, *521*, 467.

[7] A. E. Jakus, A. L. Rutz, S. W. Jordan, A. Kannan, S. M. Mitchell, C. Yun, K. D. Koube, S. C. Yoo, H. E. Whiteley, C.-P. Richter, *Sci. Transl. Med.* **2016**, *8*, 358ra127.

[8] S. Y. Chin, Y. C. Poh, A.-C. Kohler, J. T. Compton, L. L. Hsu, K. M. Lau, S. Kim, B. W. Lee, F. Y. Lee, S. K. Sia, *Sci. Robot.* **2017**, *2*, eaah6451.

[9] J. R. Raney, N. Nadkarni, C. Daraio, D. M. Kochmann, J. A. Lewis, K. Bertoldi, *Proc. Natl. Acad. Sci. USA* **2016**, *113*, 9722.

[10] A. Sydney Gladman, E. A. Matsumoto, R. G. Nuzzo, L. Mahadevan, J. A. Lewis, *Nat. Mater.* **2016**, *15*, 413.

[11] E. B. Duoss, T. H. Weisgraber, K. Hearon, C. Zhu, W. Small, T. R. Metz, J. J. Vericella, H. D. Barth, J. D. Kuntz, R. S. Maxwell, *Adv. Funct. Mater.* **2014**, *24*, 4905.

[12] a) S. Hong, D. Sycks, H. F. Chan, S. Lin, G. P. Lopez, F. Guilak, K. W. Leong, X. Zhao, *Adv. Mater.* **2015**, *27*, 4035; b) X. Liu, H. Yuk, S. Lin, G. A. Parada, T-C. Tang, E. Tham, C. Fuente-Nunez, T. K. Lu, X. Zhao, *Adv. Mater.* **2017**.

[13] D. B. Kolesky, R. L. Truby, A. Gladman, T. A. Busbee, K. A. Homan, J. A. Lewis, *Adv. Mater.* **2014**, *26*, 3124.

[14] a) T. J. Ober, D. Foresti, J. A. Lewis, *Proc. Natl. Acad. Sci. USA* **2015**, *112*, 12293; b) R. L. Truby, J. A. Lewis, *Nature* **2016**, *540*, 371.

[15] a) J. Sun, N. Phan-Thien, R. I. Tanner, *Rheol. Acta* **1996**, *35*, 1; b) R. G. Larson, P. S. Desai, *Annu. Rev. Fluid Mech.* **2015**, *47*, 47.

[16] a) N. M. Ribe, *Proc. R. Soc. London, Ser. A* **2004**, *460*, 3223; b) N. M. Ribe, M. Habibi, D. Bonn, *Annu. Rev. Fluid Mech.* **2012**, *44*, 249.

[17] a) S. W. Morris, J. H. Dawes, N. M. Ribe, J. R. Lister, *Phys. Rev. E* **2008**, *77*, 066218; b) P.-T. Brun, N. M. Ribe, B. Audoly, *Phys. Fluids* **2012**, *24*, 043102.

[18] P.-T. Brun, B. Audoly, N. M. Ribe, T. S. Eaves, J. R. Lister, *Phys. Rev. Lett.* **2015**, *114*, 174501.

[19] B. Audoly, N. Clauvelin, P.-T. Brun, M. Bergou, E. Grinspun, M. Wardetzky, *J. Comput. Phys.* **2013**, *253*, 18.

[20] M. K. Jawed, P.-T. Brun, P. M. Reis, *J. Appl. Mech.* **2015**, *82*, 121007.

[21] a) M. M. Denn, C. J. Petrie, P. Avenas, *AIChE J.* **1975**, *21*, 791; b) M. M. Denn, *Annu. Rev. Fluid Mech.* **1980**, *12*, 365; c) R. Keunings, M. J. Crochet, M. M. Denn, *Ind. Eng. Chem. Fundam.* **1983**, *22*, 347; d) T. Sridhar, R. Gupta, *J. Rheol.* **1991**, *35*, 363.

[22] a) A. Y. Malkin, C. Petrie, *J. Rheol.* **1997**, *41*, 1; b) V. Barroso, R. Andrade, J. Maia, *J. Rheol.* **2010**, *54*, 605; c) H. Tabuteau, S. Mora, G. Porte, M. Abkarian, C. Ligoure, *Phys. Rev. Lett.* **2009**, *102*, 155501; d) Q. Huang, N. J. Alvarez, A. Shabbir, O. Hassager, *Phys. Rev. Lett.* **2016**, *117*, 087801; e) Q. Huang, O. Hassager, *Soft Matter* **2017**, *13*, 3470.

[23] a) R. Passieux, L. Guthrie, S. H. Rad, M. Lévesque, D. Therriault, F. P. Gosselin, *Adv. Mater.* **2015**, *27*, 3676; b) J. Klein, M. Stern, G. Franchin, M. Kayser, C. Inamura, S. Dave, J. C. Weaver, P. Houk, P. Colombo, M. Yang, N. Oxman, *3D Print. Addit. Manuf.* **2015**, *2*, 92.

[24] U. G. Wegst, H. Bai, E. Saiz, A. P. Tomsia, R. O. Ritchie, *Nat. Mater.* **2015**, *14*, 23.

[25] S. Motte, L. J. Kaufman, *Biopolymers* **2013**, *99*, 35.

[26] J. A. Rogers, T. Someya, Y. Huang, *Science* **2010**, *327*, 1603.

[27] K.-I. Jang, H. U. Chung, S. Xu, C. H. Lee, H. Luan, J. Jeong, H. Cheng, G.-T. Kim, S. Y. Han, J. W. Lee, *Nat. Commun.* **2015**, *6*, 6566.